PERIODIC LOW ENERGY NEUTRINO SEARCH IN A HIGH ENERGY NEUTRINO DETECTOR

Research Project

BY

Jurk Katharina

Supervised by

Dr. Rodrigo Gracia Ruiz

Erlangen Centre for Astroparticle Physics
(ECAP)

Friedrich-Alexander-Universität
Erlangen-Nürnberg

May 13, 2024

PERIODIC LOW ENERGY NEUTRINO SEARCH IN A HIGH ENERGY NEUTRINO DETECTOR

Abstract

The sensitivity of neutrino telescopes depends on the energies of the interacting neutrinos. In general, the sensitivity reduces with decreasing energy as less-energetic secondaries also generate less Cherenkov photons. Most neutrino telescopes are designed to detect neutrinos in the TeV energy range. In this work, we provide a complete analysis pipeline in form of a python package to investigate the presence of low-energy periodic neutrino signals in ANTARES counting rates. We employ Epoch Folding, a method from X-ray astrophysics, as the main technique for identifying periodic signals. We provide the necessary tools to perform a sensitivity calculation for the predicted periodic neutrino flux from X-ray pulsars for ANTARES using a simulated effective volume and neutrino detection rate.

Contents

1 Introduction

Cosmic rays (CRs) are charged particles impinging on the Earth's atmosphere at a constant rate and with a nearly isotropic direction distribution. The main contribution to the CR flux comes from protons, although heavier nuclei are also present. Their energy spectrum follows a broken power law $E^{-\alpha}$ and spans over 32 orders of magnitude, reaching energies beyond the EeV scale (see Fig. 1.1).

Cosmic rays with these energies are called Ultra High Energy Cosmic Rays (UHECR), and their origin as well as the mechanisms by which they are accelerated up to these energies remain as open questions and constitute an active field of research. Models for UHECR acceleration include Gamma Ray Bursts (GRBs) and Active Galactic Nuclei (AGN) as possible sources, and predict an associated flux of high energy neutrinos (and gamma rays) resulting from the interactions of accelerated cosmic rays with matter or radiation fields in or nearby the acceleration region [1, 2].

While CRs get deflected by magnetic fields present during their propagation through the Universe, neutrinos lack electric charge and propagate in straight trajectories pointing back to their source of origin. Additionally, the comparably low cross section of neutrino interactions with matter allows them to escape from dense environments where photons would get absorbed, and to propagate cosmological distances unperturbed. These fundamental properties make neutrinos unique cosmic messengers, and the key to understand the origin of UHECR.

Detecting cosmic neutrinos on Earth is nonetheless challenging due to their low cross section and low expected flux. Although neutrino telescopes are designed to detect neutrinos with energies in the TeV range and above, it has been shown that neutrino telescopes can also be used to detect neutrinos from Supernova explosions, in the energy range ($10\,\mathrm{MeV} \lesssim E \lesssim 100\,\mathrm{MeV}$). In this project, the use of neutrino telescopes for the detection of neutrinos from periodic sources in the 10 MeV range and below is explored.

The following sections of this report will introduce optical neutrino telescopes, their detection principles and the most dominant background contributions (Sect. 2). We give an overview on the highlights of neutrino astronomy and its most prominent discoveries (Sect. 2.5). Additionally, the ANTARES neutrino telescope will be described in more detail as we will utilise its data for our analysis (Sect. 3). The detailed scientific motivation for our periodic low energy neutrino search can be found in section 4.1. Further, in section 4.3, the general analysis methods will be specified. We give a short summary on the Fast Fourier Transform method,

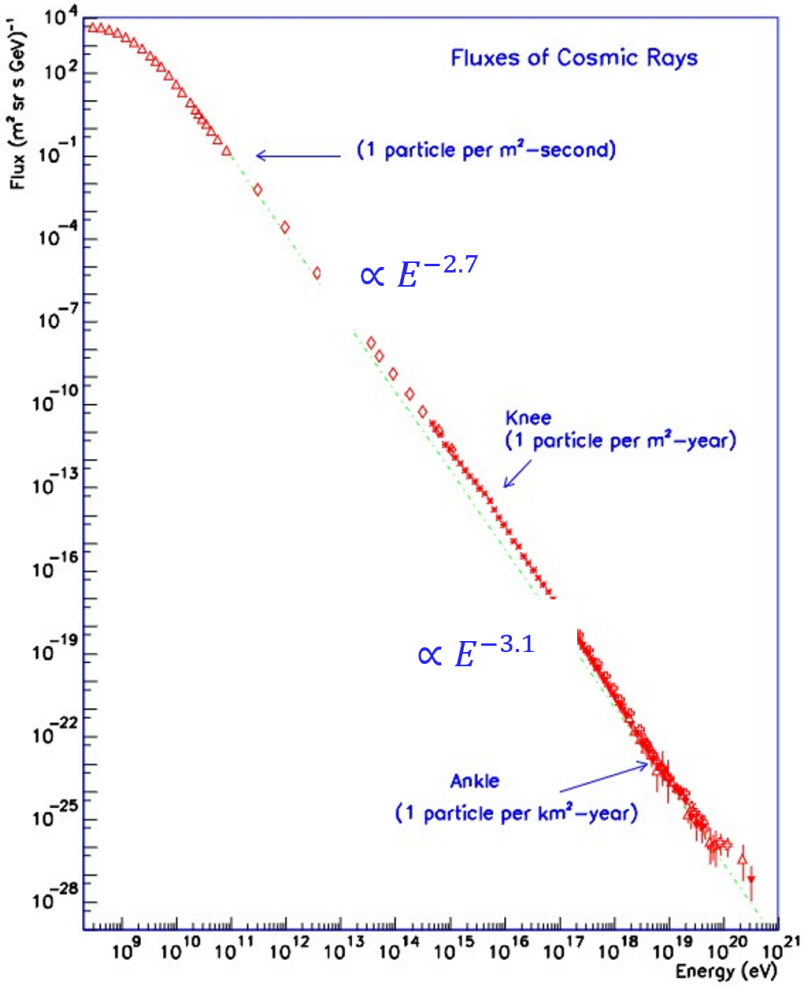

FIGURE 1.1 – Cosmic Ray flux arriving at Earth spanning over 32 orders of magnitude up to $E_{\mathrm{CR}} \lesssim 10^{21}\,\mathrm{eV}$ [4].

investigated in an earlier work [3], but then focus on Epoch Folding, the novel approach of this report. Section 5 follows with the description of the specific implementation of Epoch Folding for ANTARES data. We calculate the sensitivity of ANTARES for period low energy neutrinos based on an artificially injected signal (Sect. 6). Finally, we apply our Epoch Folding algorithm to ANTARES data (Sect. 6.4).

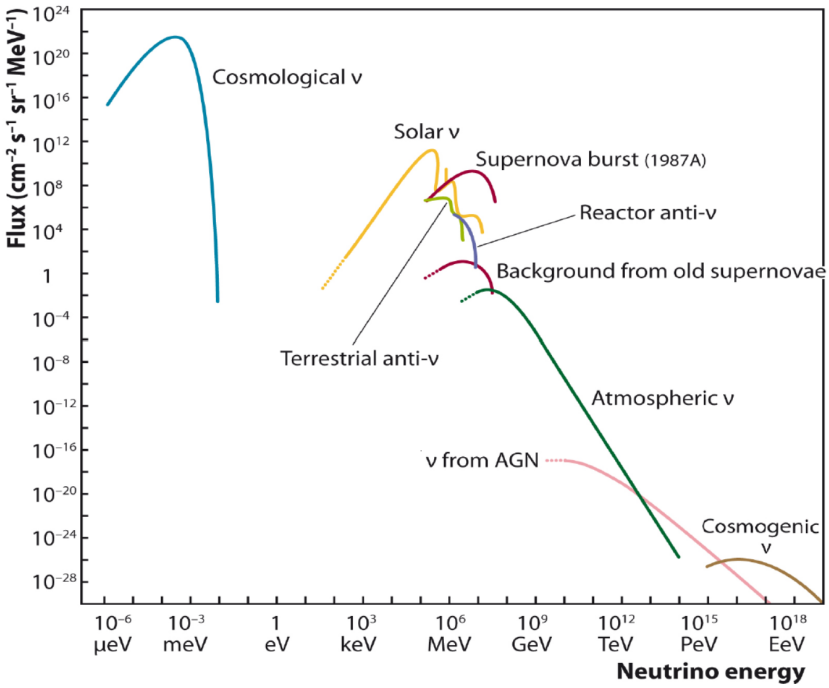

FIGURE 2.1 – Measured and predicted fluxes of neutrinos of various origin. The flux of ν from AGNs (astrophysical ν) exceeds the flux of atmospheric $\nu \gtrsim 10\,\mathrm{TeV}$ [11].

2 Neutrino telescopes

Models for neutrino emission associated to UHECR predict neutrino fluxes in the GeV up to higher than PeV energy range. An example model is shown in Figure 2.1 for the predicted AGN neutrinos at Earth, compared to neutrino fluxes from other sources. This shows that the expected cosmic neutrino flux at Earth is significantly low in itself. The low expected fluxes combined with the low cross section, make the detection of cosmic neutrinos a challenge. Additionally, Figure 2.1 shows that the so-called atmospheric neutrinos constitute a dominant source of background in the energy range where the cosmic neutrino flux is maximal. This poses an additional challenge for the detection of cosmic neutrinos.

To compensate for the low cross section and low flux, neutrino telescopes need to be built in large volumes (at least $1\,\mathrm{km}^3$ detectors are needed [5]). Neutrino telescopes are built in deep natural and transparent media such as ice at the South Pole (IceCube [6]), sea water (ANTARES [7], KM3NeT [8]) or in deep lakes such as lake Baikal in Russia (Baikal neutrino telescope [9], Baikal-GVD [10]).

2.1 Physics of neutrino interactions

Neutrinos cannot be observed directly. Instead, secondary leptons from neutrino-nucleon interactions indirectly tell us about the presence of a neutrino. These interactions can be detected when they happen inside or in the proximity of the instrumental volume of the detector.

There exist two types of neutrino-nucleon interactions: the exchange of a charged W-boson where a flavour-correlated lepton is produced – a charge-current (CC) interaction. There exist three such reactions for each flavour of the neutrino (electron, muon, tau). And the exchange of a neutral Z-boson during a neutrino-nucleon scattering process – a neutral-current (NC) interaction. For neutrino energies $\gtrsim 3$–$4\,\mathrm{GeV}$, deep inelastic scattering is the dominant contribution to the interaction cross section. In this case also a hadronic shower is produced (see Fig. 2.2).

In the detector two main event signatures can be distinguished: track-like events from ν_μ CC interactions and shower-like events from ν_l ($l = e, \mu, \tau$) NC and ν_e CC interactions. ν_τ CC interactions can be identified through a 'double-bang' signature. These events are very rare and hard to detect.

In the same manner as described above, anti-neutrinos instead of neutrinos can take part in NC and CC reactions. Antineutrinos produce the same signatures in a detector and therefore when we talk about neutrino interactions, we include both neutrinos and antineutrinos. Neutrinos also interact with electrons. Since the total interaction cross section is proportional to the target mass, electron-neutrino interactions can often be neglected.

Muon neutrino ν_μ CC interactions are referred to as the 'golden channel' for astronomy in which muons are created. Muons travel on straight trajectories through the detector medium until an interaction changes their direction. The range of a charged lepton gives its average distance traversed before experiencing energy loss by interacting or decaying [12]. Compared to electrons and taus, muons have the longest range (e.g., $1\,\mathrm{km}$ @ $250\,\mathrm{GeV}$ in water [13]). Therefore Cherenkov photons from ν_μ interactions can also be detected even if the interaction vertex is further away from the instrumental volume of the detector increasing its detection probability. The angle between the neutrino and the outgoing lepton depends on the neutrino energy. At high energies, muons from CC interactions are produced co-linear to the original neutrino direction, hence they point directly to the direction of the neutrino source [13, 14].

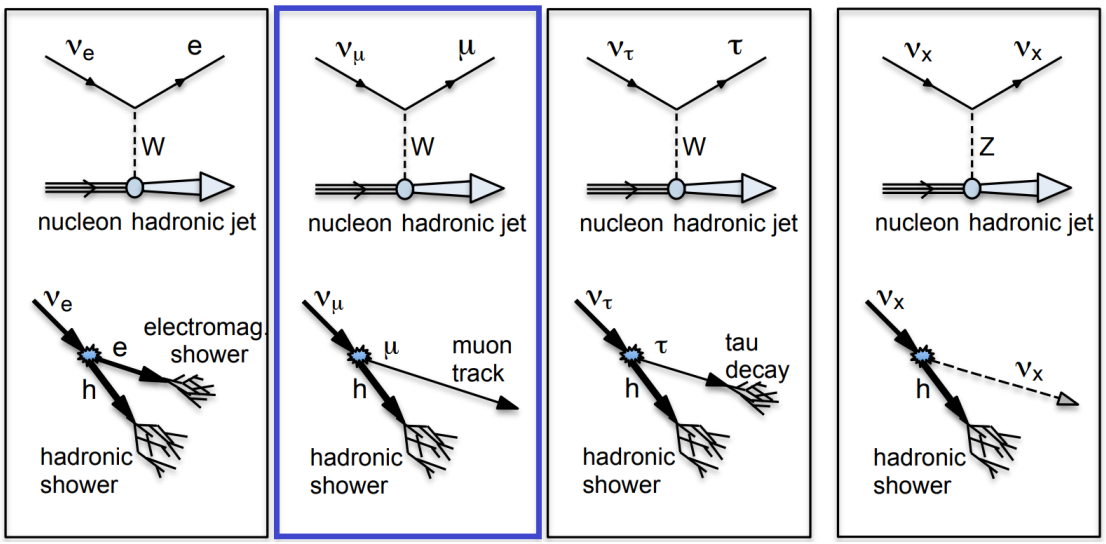

FIGURE 2.2 – Different neutrino-nucleon interactions with schematic Feynman diagrams (top) and event signatures in detectors (bottom). The first three panels show charged current (CC) interactions, the exchange of a charged boson ($W^{\pm}$). The last panel depicts a neutral current (NC) interaction, the exchange of the neutral Z-boson. Muon neutrino CC interactions are most useful for neutrino astronomy [13].

2.2 Cherenkov radiation

Relativistic charged particles propagating in a dielectric medium (e.g., water or ice) with velocities v_p higher than the phase velocity of electromagnetic radiation c_n in the medium polarise the medium around them and excite particles therein. In the process of de-excitation, the particles emit Cherenkov radiation. The overlapping of consequent spherical wavefronts of electromagnetic fields and their constructive interference lead to the characteristic cone shape (see Fig. 2.4). The resulting effective wavefront travels in the direction given by the emission angle θ_C. The emission angle θ_C of the Cherenkov photons depends on the original particle's velocity v_p and the refractive index $n(\lambda)$ of the dielectric medium at a certain wavelength λ. Simple geometric and trigonometric considerations (Fig. 2.4) yield [15]

$$\cos\theta_\mathrm{C} = \frac{1}{n(\lambda)\beta}, \text{ where } \beta = \frac{v_\mathrm{p}}{c}. \tag{2.1}$$

For relativistic particles ($\beta \approx 1$) moving in water at a temperature $T = 20\,^\circ\mathrm{C}$ ($n_\mathrm{water} \approx 1.34$), the emission angle of Cherenkov photons of $\lambda = 400\,\mathrm{nm}$ is $\theta_\mathrm{C} \approx 42\,^\circ$. The spectral density of emitted Cherenkov radiation is given by [16]:

$$\frac{d^2N}{dxd\lambda} = \frac{2\pi\alpha}{\lambda^2}\left(1 - \frac{1}{\beta^2 n(\lambda)^2}\right) \tag{2.2}$$

The spectrum decreases with increasing wavelength with the highest number of photons produced in the UV regime. For neutrino telescopes, absorption and scattering of photons in the detector medium have to be considered. UV radiation is absorbed by water (and thus also ice) molecules. Scattering effects are much less prominent in water than in ice. Considering these effects, the relevant wavelength range for photomultiplier tubes is between 300 and 600 nm [13, 14].

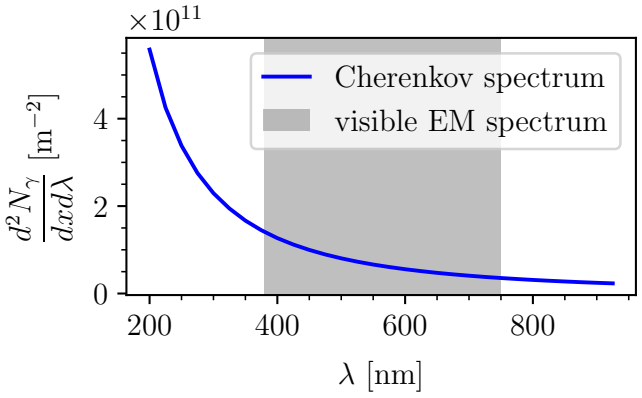

FIGURE 2.3 – Spectral density of Cherenkov radiation with the refractive index of water $n_{\text{water}}(\lambda)$ at $T = 25\,°\text{C}$ (without extinction). The dependency of the refractive index was adopted from [17].

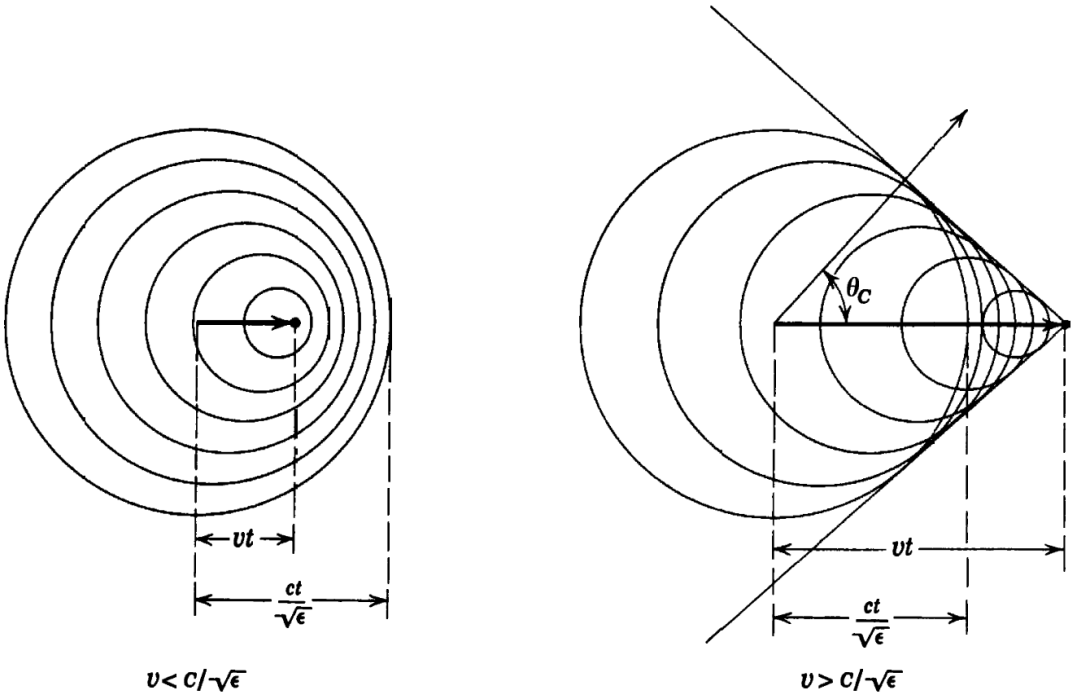

FIGURE 2.4 – Wavefronts of electromagnetic fields induced by a particle travelling less than (left) and greater than the velocity of light in the medium $c_n = c/n = c/\sqrt{\epsilon}$ (the refractive index n can alternatively be described with the dielectric constant $\epsilon(\lambda)$). Only for $v_\text{p} > c_n$, constructive interference produces the Cherenkov cone. The resulting wavefronts move in the direction of the Cherenkov angle θ_C [18].

2.3 Detection principle

Neutrino telescopes are three-dimensional arrays of photomultiplier tubes (PMTs) designed to detect Cherenkov radiation produced by the propagation of charged particles emerging from neutrino interactions with matter.

These Cherenkov photons produce 'hits' in the PMTs. From the 'hit' positions and times, the arrival time and direction of neutrinos can be reconstructed. The summed-up 'hit' charge indicates the particle's energy.

The sensitivity of neutrino telescopes depends on the energies of the interacting neutrinos. It can be described by the so-called effective area $A_{\text{eff}}(E)$, which is defined as the ratio between the neutrino detection rate and the incoming neutrino flux [19]. The instruments are designed to maximise their $A_{\text{eff}}(E)$ in the energy range relevant to their scientific motivation. A more detailed discussion on the energy dependence of the effective area can be found in section 3.

2.4 Atmospheric background and analysis methods

The greatest obstacle for performing neutrino astronomy from Earth is the Earth's atmosphere. Cherenkov radiation is not only produced by secondaries from cosmic neutrino interactions, but also atmospheric neutrinos and muons.

Cosmic rays interact with matter in the atmosphere and produce leptonic and hadronic showers. The outgoing neutrinos as well as the muons can propagate several kilometres deep and reach the detector site, producing unwanted signal.

Neutrino telescopes can eliminate 'up-going' muons which would reach the detector from below. As they would need to propagate through the Earth first, they get absorbed before reaching the detector volume. 'Down-going' muons – those reaching the detector from above – cannot be as easily filtered out. Several strategies are employed to handle this background (see, e.g., [20]).

As shown in Figure 2.1, the atmospheric neutrino flux is a non negligible source of background for neutrino telescopes. These neutrinos are produced upon CR interactions in the atmosphere [1, 2].

Unlike muons, up-going neutrinos can traverse Earth with a negligible absorption probability [14]. Even though, at sufficiently high energies also neutrinos will be absorbed by the Earth [19].

In order to discriminate signal from background events, different analysis strategies can be applied. The most relevant three methods to distinguish cosmic and atmospheric neutrinos are: firstly, astrophysical and atmospheric neutrinos differ for example in their energy spectrum. Models predict that the flux of cosmic

neutrinos exceeds the one of atmospheric neutrinos above 10 TeV [20, and references therein]. Hence, a high number of events at the highest energies would be attributed rather to cosmic than atmospheric neutrinos. Secondly, CRs arrive at Earth from all directions and thus atmospheric neutrinos are produced almost uniformly other the entire sky. An excess of events in a certain location at a certain time in the detector, can single out neutrinos from an astrophysical source. Thirdly, as neutrinos are produced together with CRs and electromagnetic radiation, coincident detections of neutrinos in multiple neutrino telescopes, CRs or high-energy photons can identify cosmic neutrinos.

2.5 Highlights from neutrino astronomy

Nowadays, the field of Neutrino Astronomy has advanced to the point that it is not only a tool to investigate the origin of CRs, but an independent research area to understand origins of neutrinos themselves. Over years several telescopes have been built and/or will be extended. ANTARES, KM3NeT, IceCube and the telescopes in lake Baikal all share the properties described in the previous sections. All relevant results in neutrino astronomy to date have been achieved by the IceCube Collaboration.

There exist a number of astrophysical sources predicted to emit neutrinos: gamma-ray bursts, active galactic nuclei, blazars, starburst galaxies, supernovae, supernova remnants and pulsars [21], [20], [22]. So far, using the methods described in section 2.4 four major neutrino sources have been confirmed. In 2013, an extragalactic diffuse neutrino flux – not attributed to any specific object – was reported [23]. Two examples of successful cooperation in multi-messenger astronomy are the blazar TXS 0506+056 and the active galaxy NGC 1068. In 2017 a high-energy neutrino from TXS 0506+056 was detected coincidentally with a gamma-ray flare confirming blazars as neutrino sources [24]. NGC 1068 followed in 2022 with an excess of TeV neutrinos [25]. The most recent discovery reports the observation of a significant number of neutrinos from the Galactic plane using machine learning techniques over a 10 year data taking period [26].

3 ANTARES – a high energy neutrino telescope

Astronomy with a Neutrino Telescope and Abyss environmental RESearch, short ANTARES, was a water Cherenkov detector in the Mediterranean Sea located 40 km offshore from Toulon in France at 2475 m depth [27]. It was operational

and taking data from May, 2008, until February, 2022. Its successor, KM3NeT, is currently being constructed in two locations close to France and Italy.

ANTARES is designed to detect high energy neutrinos in the energy range ($10\,\mathrm{GeV} \lesssim E_\nu \lesssim 100\,\mathrm{TeV}$). Cherenkov radiation is detected with a 3-dimensional matrix of photomultiplier tubes (PMTs) contained in glass spheres, so-called Optical Modules (OMs). Three OMs are in turn attached to storeys, called Optical Module Frames (OMFs) (see Fig. 3.1b). 25 of such OMFs are combined to one detector line with a spacing of 14.5 m. The full telescope consists of 12 lines and 885 OMs. A schematic view of the entire detector is shown in Fig. 3.1a.

ANTARES is optimised to detect up-going neutrinos while using the Earth as a natural shield to reduce the contamination of atmospheric muons (see Fig. 3.2). Thus, the detector's location on the Northern Hemisphere makes ANTARES sensitive to sources in the Southern Hemisphere including many Galactic sources as well as the Galactic Center.

In addition, 'hits' are not only produced by Cherenkov photons, but also other processes in the detector medium. All these effects combined produce a background in the neutrino detector that has to be filtered out or accounted for when searching for the actually desired signal – cosmic neutrinos. Computer algorithms are used which recognise physically interesting events by time correlating photon 'hits' between different photomultipliers. These 'hits' are then recorded as 'events'.

The effective area introduced in section 2.3 describes the ability of a neutrino telescope to detect neutrinos of a certain flavour, energy and direction. In general, the effective area reduces with decreasing energy since a low-energy incoming particle also produces a low-energy secondary (see Fig. 3.3). Lower-energy secondaries travel less distance and therefore emit Cherenkov photons on a shorter path through the detector than higher-energy secondaries. As a result, the photons are recorded by less photomultipliers and the efficiency of identifying neutrino events reduces. Neutrino telescopes like ANTARES are optimised to detect neutrinos in the TeV range and above. For this, one needs to instrument a volume as large as possible. With a fixed number of OMs, one can achieve this at the cost of increasing the average distance between the OMs, and therefore decreasing the efficiency for detecting neutrinos of lower energies, as can be seen in Figure 3.3.

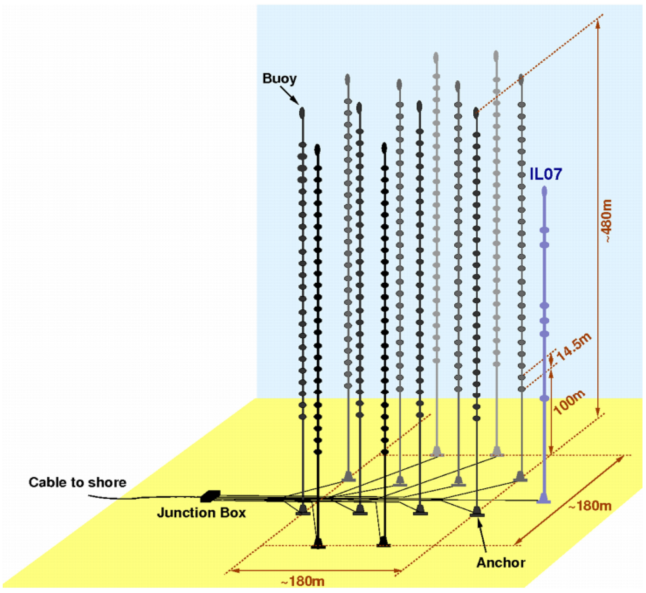

(A) Schematic view of the ANTARES detector (after [27]).

(B) An Optical Module Frame (OMF) from the ANTARES telescope. Now, an exhibition piece at ECAP.

FIGURE 3.1 – ANTARES neutrino telescope.

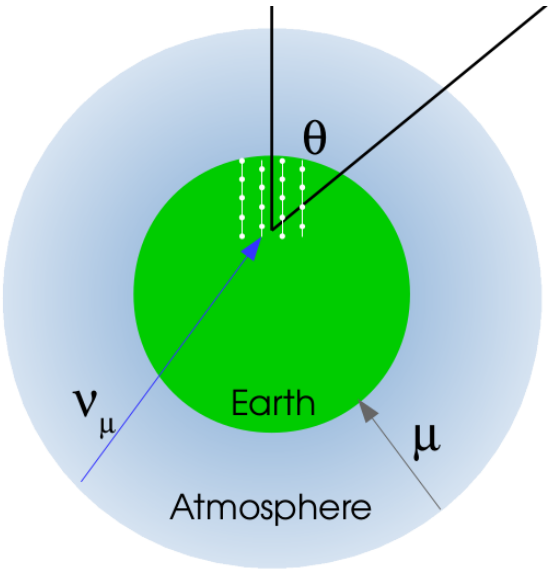

FIGURE 3.2 – Schematic representation of 'up-going' neutrinos and muons. While muons are absorbed in the Earth, neutrinos still reach the detector. θ is the so-called zenith angle used to express the direction of incoming particles into the neutrino detector [12].

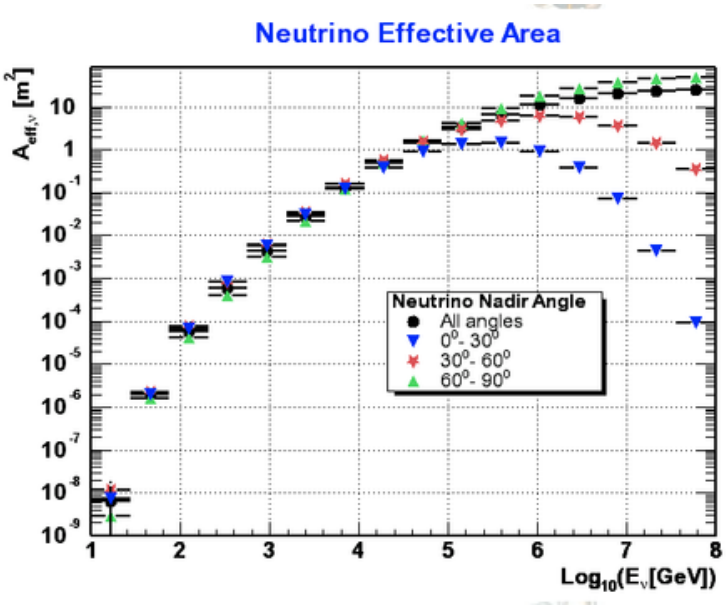

FIGURE 3.3 – Effective Area of ANTARES. Credit: ANTARES Collaboration.

3.1 Optical Background

Besides the atmospheric background events described in section 2.4, the ANTARES detector suffered from the so-called optical background. The medium that the detector is placed in comprises additional challenges. For the ANTARES telescope, two effects in the Mediterranean Sea dominate the PMT rates. Firstly, the radioactive decay of the potassium-40 isotopes ^{40}K and the subsequent Cherenkov emission from decay electrons adds an approximately constant background rate. Secondly, marine bio-luminescence adds a season-dependent variable background rate with an approximate yearly period (see Fig. 3.4). This bio-luminescent light emission is not well understood and thus not easy to model.

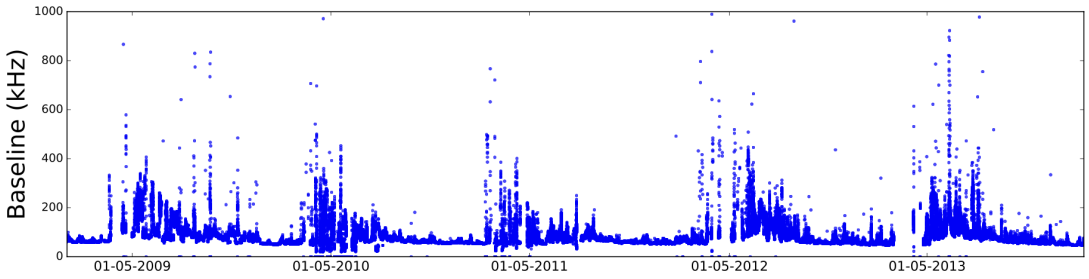

FIGURE 3.4 – ANTARES PMT rates over the course of 5 years. The yearly spikes in the data are due to the increased bio-luminescence production in spring [12].

4 Search for low energy neutrinos from periodic sources

4.1 Motivation

Our main motivation comes from a technical point of view, namely the working principle of the detector. Under certain circumstances, neutrinos with lower energies than the range at which the detector was designed for, can be detected by using the OMs as independent detectors. The counting rate of a OM is dominated by the optical background. A flux of low energy neutrinos could be detected if they produce a pattern different from the optical background. Two possible scenarios that are discussed in literature are, firstly, core-collapse Supernovae. Neutrinos from such explosions would produce a generalised increase of the PMT counting rates during the Supernova. This analysis is pursued by the KM3NeT collaboration [28]. Secondly, another possibility would be to search for periodic patterns in the counting rates on time scales of variable astrophysical sources. One of the astrophysical objects predicted to emit such periodic low-energy neutrinos are binary pulsars [29, and references therein].

In this work we explore the possibility of using the photon rates recorded by ANTARES to search for low-energy neutrinos despite the reduced efficiency of the detector. As such we do not rely on the combination of multiple PMTs and algorithms to pre-select events, but use the single OMs as standalone neutrino detectors.

4.2 Candidate sources: Binary pulsars

Pulsars are highly magnetised neutron stars with magnetic field strengths of around 10^8 T. Pulsars are formed in supernova explosions of massive stars ($M \gtrsim 8\,\mathrm{M}_\odot$) when the original star ejects its mass and the collapsed core remains as a neutron star. Typically, neutron stars have masses around 2–3 $\mathrm{M}_\odot$ and sizes of about $D = 10$ km. The progenitor star's rotation in combination with the reduction in size increases the resulting neutron star's magnetic field strength and spin.

Due to these high rotation speeds, relativistic particles will emit radiation along the magnetic field lines in a cone in their direction of motion. Historically, pulsars were discovered through the observation of pulsed radio emission as the magnetic and rotational axes are misaligned.

When pulsars are found in close binary systems, they accrete matter from their companion star. The accreted material follows the neutron star's magnetic field lines and forms accretion columns in which X-ray photons are generated. It is observed that binary pulsars show pulsations in X-rays instead of radio. And their spin periods are usually in the range of seconds.

If the mass accretion rate becomes very high, e.g., during high-mass accreting phases called outbursts, the temperature inside of the accretion columns increases up to 1 MeV and photons no longer can escape from the accretion column flow fast enough (see Fig. 4.1). Instead the photon is converted into an electron-positron pair. Pair annihilation then causes neutrino emission: $e^- e^+ \to \nu\overline{\nu}$. For more details on the model, please see [29] or [22].

The predicted neutrinos from binary pulsars (BP) have energies in the MeV energy range. The predicted neutrino flux at Earth is of the order of $\sim 10^{-5}\,\mathrm{MeV\,cm^{-2}\,s^{-1}}$. A comparison of BP neutrino flux with other neutrino sources is shown in figure 4.2. The expected BP neutrino flux is at least two orders of magnitude lower than the isotropic flux from the nuclear reaction in stars inside the Galaxy.

In this work, we assume the neutrino signal will be pulsed in the same way as the photon radiation as the neutrinos are predicted to be produced in accretion columns following the magnetic fields and thus misaligned to the pulsar's rotation axis. Hence, we optimise our analysis pipeline for the search of periodic signals from low-energy neutrino fluxes.

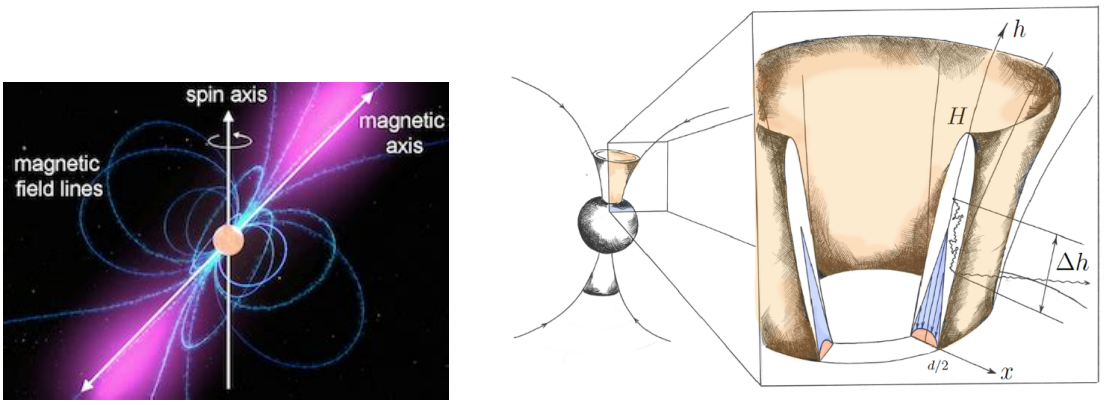

FIGURE 4.1 – (Left) Schematic of a radio pulsar with the misaligned spin and magnetic axes, magnetic field lines (blue) and beamed radiation cones (magenta). Credit: NASA/Goddard Space Flight Center Conceptual Image Lab. (Right) Schematic view of an accreting pulsar and its accretion columns. The orange shaded area shows the region of neutrino production [29].

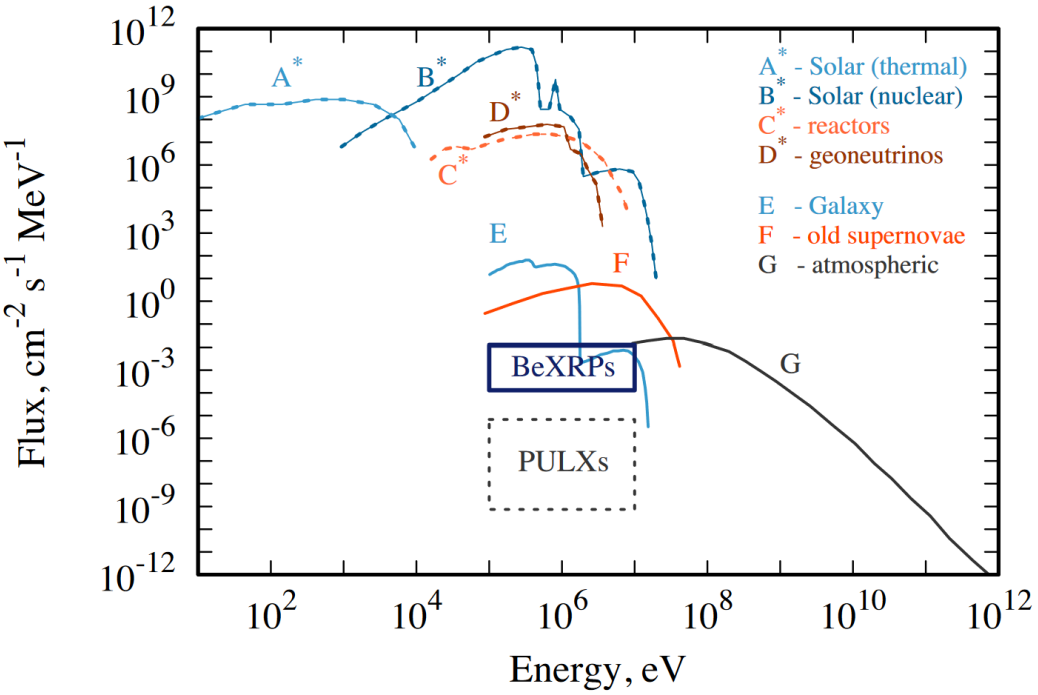

FIGURE 4.2 – Comparison of the neutrino flux at Earth from binary pulsars (Be XRPs and PULXs) and various other sources [22]. The significantly lower neutrino flux from such systems is evident.

4.3 Methods for Timing Analyses

In X-ray astrophysics, the detection of a photon is registered with at least three properties: its arrival time, energy and position in a detector – we call this an event (count). The combination of all photons detected in a certain observation is then called eventlist. When the single photons are binned over time, we obtain a lightcurve – a count rate over time. The lightcurve enables us to study the flux evolution of an astrophysical X-ray source. For our purpose, detecting a periodic signal over time, we are only interested in the arrival times of photons in a certain time period – the eventlist.

4.3.1 First Approach – Fast Fourier Transform

The first technique that was used to develop an analysis technique for neutrino telescope data is the Fast Fourier Transform (FFT). This standard technique in timing analyses converts the original dataset in the time domain into frequency space using the Fourier transformation (FT). The advantage of using the FFT is that unknown frequencies of periodic signals can be easily identified, also in noise-dominated data (see Fig. 4.3 and Fig. 4.4). Since the FT represents the original data as a sum of multiple sine and cosine functions, periodic signals with sinusoidal shapes are more easily identified.

One major downfall of using FFT on a large dataset is the necessity of the entire dataset being accessible to the FFT. Performing the FFT on small subsets and combining the FT power spectra, reduces the sensitivity of the detection as the combination averages over the single power spectra.

For more details on the implementation of the FFT technique on ANTARES data, see [3].

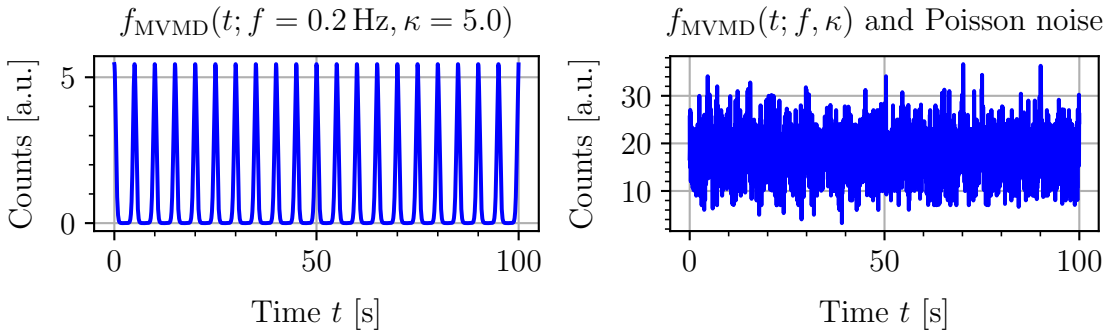

FIGURE 4.3 – (Left) An example lightcurve for a pulsation of frequency $f = 0.2\,\mathrm{Hz}$. The pulse shape follows the modified von Mises distribution (MVMD, see Sect. 6.2.1) with shape parameter $\kappa = 5$. (Right) The same lightcurve, but with Poisson distributed noise added to the signal.

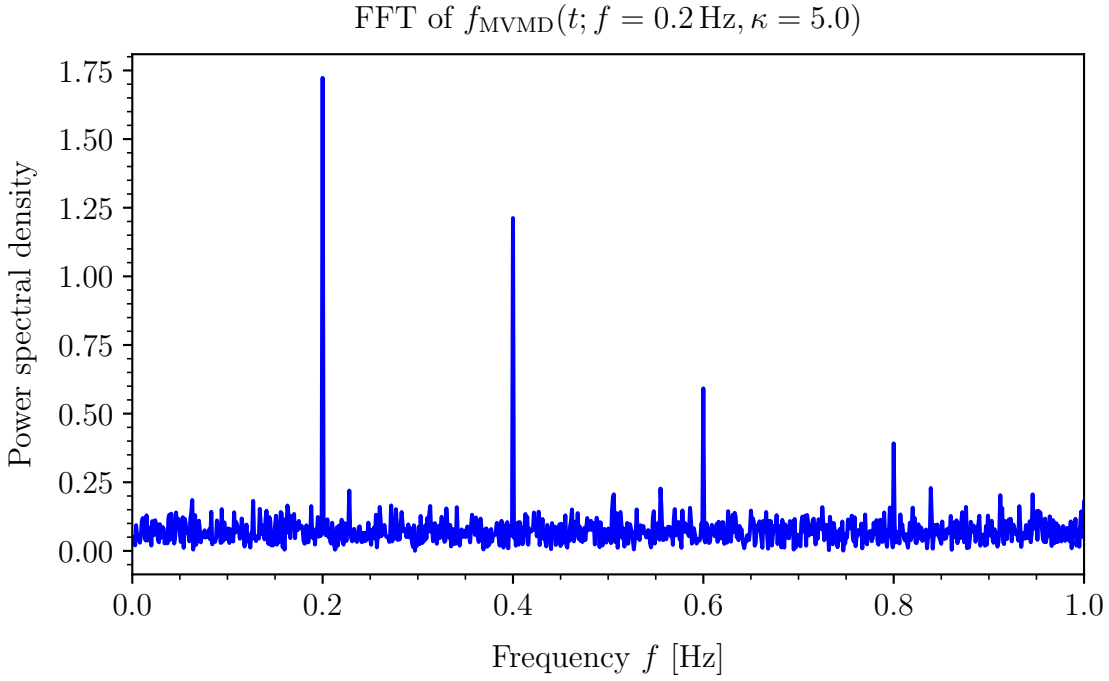

FIGURE 4.4 – FFT of the signal in Figure 4.3. As the MVMD can be represented as a sum of sinusoids, we see peaks at multiples of the principal frequency $f = 0.2\,\mathrm{Hz}$.

4.3.2 New Approach – Epoch Folding

A second method for identifying periodic signals is named epoch folding [30, 31]. The idea of epoch folding is conceptually very simple: we divide our dataset into sections ('epochs') with a certain test-frequency and add ('fold') the signals in each section. On the one hand, if the test-frequency corresponds to the actual period of the signal, the periodic signal is amplified, whereas the noise is averaged out, making it possible to identify the periodic signal. On the other hand, if the test-frequency does not correspond to the real period, the folded profile will be averaged to a mean count rate and resemble a 'flat' distribution (see Fig. 4.5). This method is therefore also more sensitive to arbitrarily shaped signals compared to the FFT. In general, utilising Epoch Folding for a periodic search requires less data pre-processing than with the FFT.

In the following, a more sophisticated view on the principle behind the epoch folding method is given [32, 33]. The periods of pulsars are not constant in time but can vary due to rotational energy loss. The pulse frequency can be expanded as a Taylor series [33]:

$$f(t) = \sum_{n=0}^{\infty} \frac{t^n}{n!} \frac{d^n f}{dt} \tag{4.1}$$

$$= f + \dot{f} \cdot t + \frac{1}{2} \cdot \ddot{f} \cdot t^2 + \dots \,, \tag{4.2}$$

The pulse phase is for a certain frequency f defined as $\varphi = f \cdot t$. For a time varying frequency $f(t)$, the pulse phase can then be equally expanded as [33]:

$$\varphi(t; f(t)) = \sum_{n=1}^{\infty} \frac{t^n}{n!} \frac{d^{(n-1)} f(t)}{dt} \tag{4.3}$$

$$= f \cdot t + \frac{1}{2} \cdot \dot{f} \cdot t^2 + \dots \tag{4.4}$$

In epoch folding, we work in phase instead of time space. The time t in equation (4.4) represents the photon arrival times t_{photon} and the frequency f is the test-frequency f_{test}:

$$\varphi\left(t; f_{\text{test}}; \frac{d^{(n)} f(t)}{dt}\right) = f_{\text{test}} \cdot t + \frac{1}{2} \cdot \dot{f} \cdot t^2 + \dots \tag{4.5}$$

where $n \geqslant 1$ gives the degree of derivation. The phase shift φ_{ef} is given as the

fractional part of the phase φ as defined in (4.5), so that it is normalised $0 \leqslant \varphi_{\mathrm{ef}} \leqslant 1$:

$$\varphi_{\mathrm{ef}}\left(t; f_{\mathrm{test}}; \frac{d^{(n)} f(t)}{dt}\right) = \varphi - \lfloor \varphi \rfloor. \tag{4.6}$$

The actual folding operation consists of assuming a test-frequency and sorting the photon arrival times into a pulse phase histogram with N bins. The number of events x_j contributing to one pulse phase bin H_i with $0 \leqslant i \leqslant N-1$ is:

$$H_i = c_i \sum_{j=0}^{M} x_j \text{ with } x_j \begin{cases} 1, & \text{if } i/N \leqslant \varphi_{\mathrm{ef}} \leqslant (i+1)/N \\ 0, & \text{else} \end{cases}, \tag{4.7}$$

where c is a normalising factor, M is the total number of events in the eventlist and φ_{ef} as in (4.6). If the test-frequency f_{test} matches the frequency f_{true} of an oscillation present in the signal, the pulse phase histogram H will show the pulse profile. If $f_{\mathrm{true}} \neq f_{\mathrm{test}}$, the histogram H will be averaged to a constant mean number of photons (see Fig. 4.5).

To quantify the above described observation, we test the number of events in one pulse phase bin H_i against a constant profile using a χ^2-test [34]. The epoch folding test statistic is calculated as follows:

$$\chi^2 = \sum_{i=0}^{N} \frac{H_i - \langle H \rangle}{\sigma_H^2} \text{ with } \sigma_H = \sqrt{\langle H \rangle}, \tag{4.8}$$

where $\langle H \rangle$ is the mean and σ_H the standard deviation (under the assumption of Poisson distributed folded events) of pulse phase histogram H.

Using a χ^2-test is appropriate for a sufficiently long time series [35]. This condition is given for the ANTARES data we will analyse (see Sect. 5.2.2).

To search for oscillations, the pulse phase histogram H and the χ^2 test statistic is calculated for a range of test-frequencies. The resulting χ^2 landscape will have (at least) a maximum at the pulse frequency of the pulsar where the hypothesis of a constant profile will be maximally violated [32].

A disadvantage of Epoch Folding is that the true frequency of the oscillation should be known as the test statistic can show a maximum at half the oscillation frequency instead of the actual frequency [32]. It is therefore not suited for searches of periodic signals of unknown frequency, but instead to determine whether an oscillation is present.

Due to the conversion of times t into pulse phases φ, gaps in a dataset do not

introduce potentially complicated features as for the FFT [32]. A lightcurve (or eventlist) does not have to be separated into segments and hence, the precision of the determined pulse frequency is increased [32]. Nevertheless, the presence of 'bad time intervals' reduces the total integration time of the observation and the integration time of a single bin in the pulse phase histogram H. The bins H_i should therefore be weighted to account for an uneven integration time in each bin [30]. This is taken into account in equation (4.7) with the normalising factor c_i. Although this feature of incorporating 'good time intervals' and the normalisation of the pulse phase histogram is currently implemented in our code, it does not produce the desired outcome. More details can be found in Section 5.3.

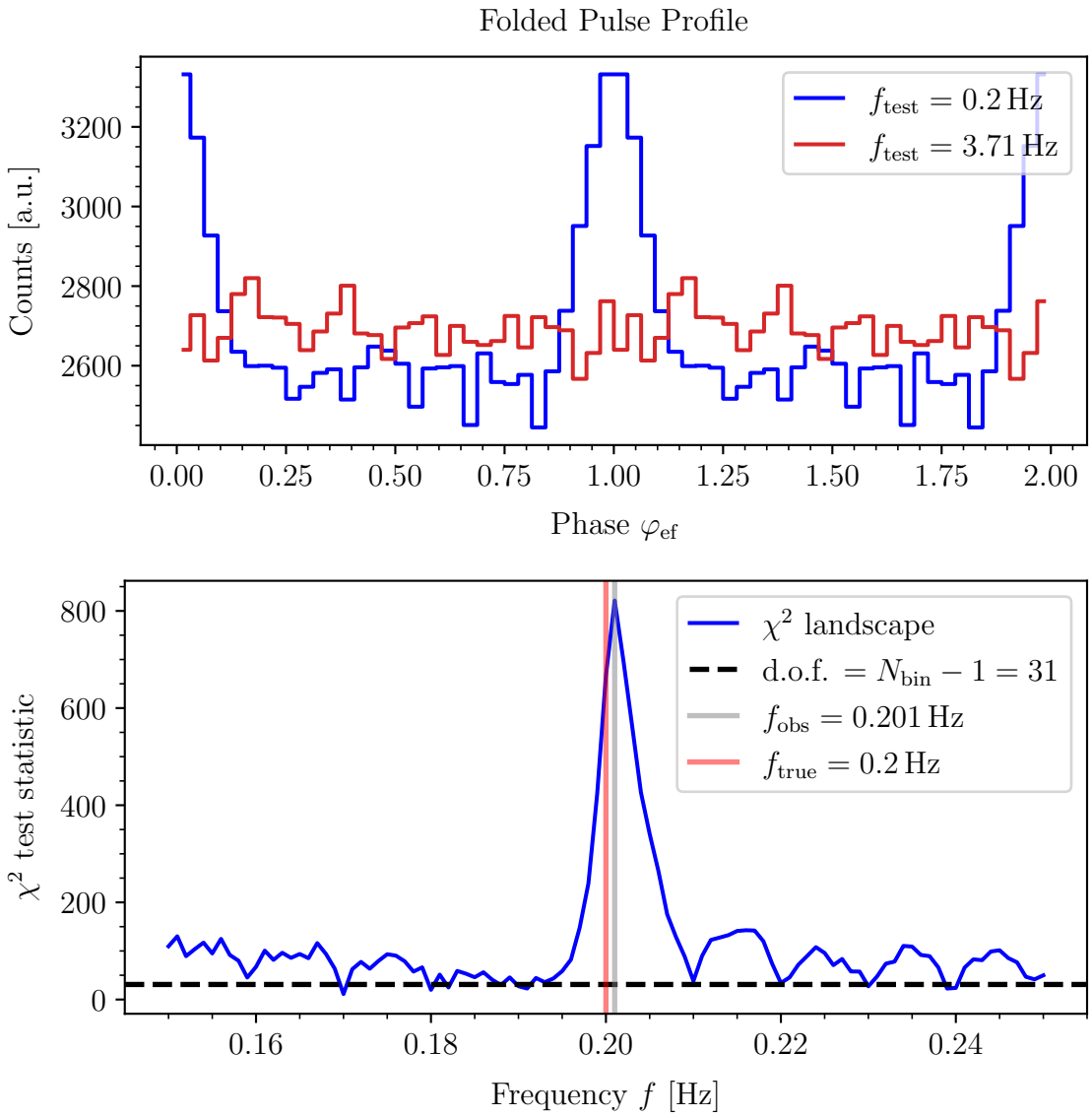

FIGURE 4.5 – Epoch Folding applied on the noisy lightcurve in Figure 4.3. (Top) The folded profile for two different test-frequencies. For the true frequency, a pulse is visible, whereas for $f = 3.71\,\text{Hz}$ the profile is averaged to a mean count number. (Bottom) The χ^2 landscape for a range of test-frequencies $0.15 \leqslant f_{\text{test}} \leqslant 0.25$ showing a maximum around the true frequency.

5 Implementation of Epoch Folding for ANTARES data

5.1 General ANTARES data handling

Data blinding is a standard practice in particle physics, cosmology and also neutrino astronomy, to avoid potential bias and errors in analysis results. Hence, before applying any analysis on the real un-blinded ANTARES data, the methods are tested on randomised data. After a successful review of the blinded analysis by the ANTARES collaboration, the study can be performed on the original un-blinded data.

For analyses for which un-randomised data is required, the ANTARES collaboration allows to use 0-ending runs – a small subset of the entire data sample. We utilise 0-ending runs (0 runs in the following) to understand the behaviour of the ANTARES optical background in our epoch folding pipeline.

5.2 Data Pre-processing

Due to the expected large dataset of to be analysed ANTARES data, observational effects due to the motion of the Earth and the binary pulsar and the standards of X-ray timing analyses, it was necessary to pre-process the data before applying the epoch folding analysis.

5.2.1 Eventlist Creation

The ANTARES data is available to us as PMT counting rates. Hence, we start with a lightcurve with a bin size of around 100 ms. However, the epoch folding technique employed in X-ray astronomy, is performed on an eventlist. Therefore, it is necessary to convert the ANTARES PMT rates into an eventlist.

Since this requires information about the exact number and distribution of photon arrival times ('hits') inside the 100 ms time intervals which we do not have, we need to make an assumption. We assume a uniform distribution of PMT 'hits' inside each 100 ms time interval. The number of 'hits' is then given by the countrate inside the corresponding bin.

5.2.2 Data Splitting and Scaling

ANTARES data is not recorded continuously, but in larger time intervals. The recorded detector 'hits' inside these time intervals (between 8 and 12 hours) are binned into total PMT rates (all PMTs combined). One such data recording interval is called a 'run'. A histogram showing the distribution of total rates for a 0-run is displayed in Figure 5.1. Since the time period for the final analysis is about 150 days (see Sect. 6.4), multiple runs have to be combined for the analysis. Due to the very high background, the single PMT counting rates are in the kHz regime. Already, a dataset with the size of the multiple-runs combined PMT rates would be too computationally and time intensive. Hence, the single ANTARES runs are analysed separately.

Since for the epoch folding technique, we are transforming the kHz count rates into single events, this, additionally, increases the dataset of a single run to a number of photon events of (mean count rate) × (length of a single run). For $\lesssim 12\,\mathrm{h}$ long run and a $\sim 10^4\,\mathrm{kHz}$ count rate, this would result in $\lesssim 10^{14}$ events. Therefore, we on one hand split a run into further subsets to decrease the number of bins. On the other hand, we rescale the kHz PMT rates, so that instead of millions of photons inside a 100 ms time bin, we only generate ~10–10^2. This factor has to be accounted for again later when we calculate the sensitivity of the detector from the strength of an artificially injected periodic signal (more details follow in Sect. 6.2).

Due to the principle of epoch folding, this does not pose any problems. To obtain the final folded profile for a certain test-frequency, the folded profiles of each split are added together independently of the split and run.

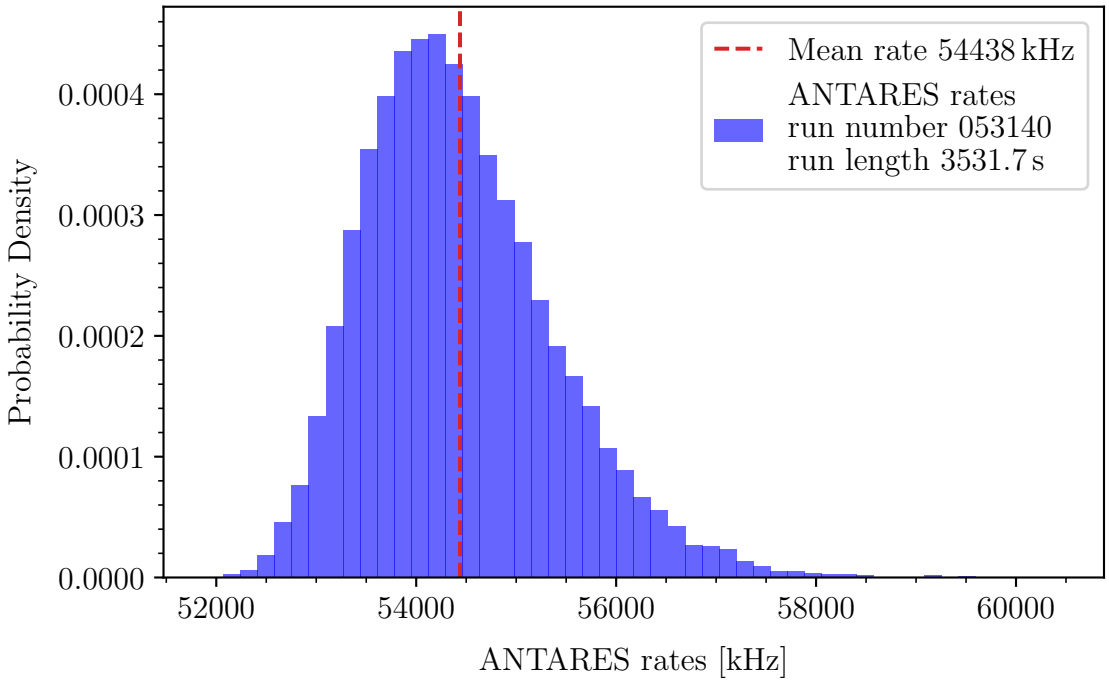

FIGURE 5.1 – Histogram of total PMT rates for data run number 053140.

5.2.3 Relative motion corrections

Due to the relative motion of the Earth and hence the ANTARES detector and the neutrino source – the pulsar, the arrival times of neutrinos and therefore Cherenkov photons are shifted, distorting the original pulse shape. The barycentric and binary corrections account for these effects.

Barycentric Correction The motion of the Earth around the Sun introduces a shift in the photon arrival times detected from an astrophysical source. This can be corrected for with a coordinate transformation from the rotating frame of the Earth to a non-rotating (inertial) frame, here, the barycenter of the Solar System. The barycenter is the center of mass of multiple gravitationally interacting objects orbiting each other. Hence, it defines the point which all bodies in the system orbit.

Instead of using the photon arrival times recorded on Earth which is changing its position, we mathematically transfer the location of our detector at the time of our observation to the barycenter of the Solar System (SSB). This takes the projected photon travel time to the SSB into account.

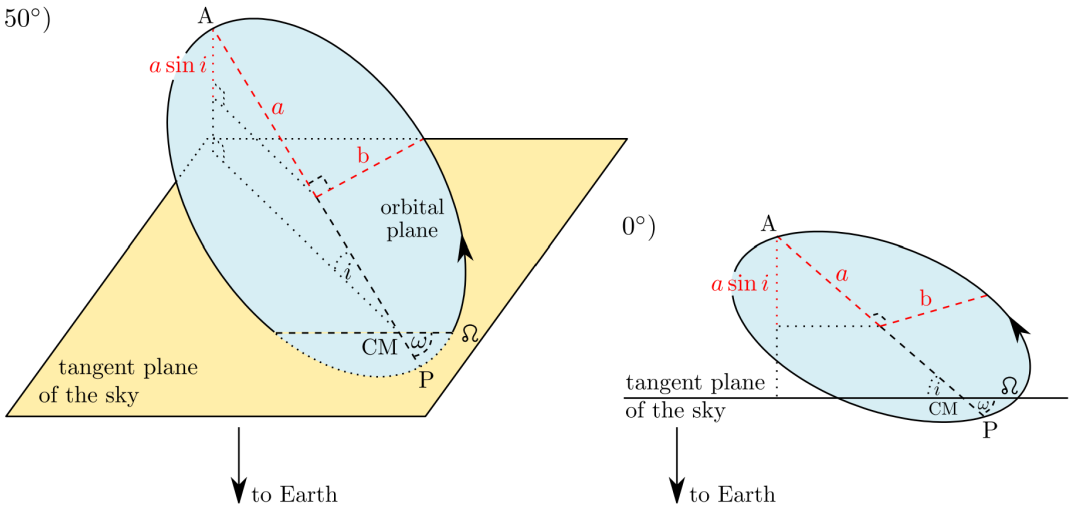

FIGURE 5.2 – Illustration of the orbit of a neutron star around the center of mass (CM) in a binary system viewed from two different angles (50 ° and 0 °) and the definition of orbital parameters. The observer is looking at the binary system from below the tangent plane [32].

Binary Correction Following the model of neutrino emission in binary pulsars, similarly to the barycentric correction, we need to correct for the motion of the pulsar in the binary system as well. The observed pulse period of the pulsar is effected by the Doppler shift causing a time delay Δt_{orbit} in the photon arrival times in the detector. This time delay is given by the light-travel-time – the time it takes for a photon to travel from the current position of the pulsar across the orbit projection into the observer's line of sight [33].

The light travel time due to the neutron star's motion in a binary system can then be calculated from the line-of-sight displacement Δz to first order in e [36]:

$$\Delta t_{\text{orbit}} = \frac{\Delta z}{c} \approx x \left(\sin(M + \omega) - \frac{3}{2} e \sin\omega + \frac{1}{2} e \sin(2M + \omega) \right) \tag{5.1}$$

with $x = a \sin(i)/c$ the projected semi-major axis (in time units) and other parameters as defined in Table 5.1.

The above described corrections are not the only factors causing a change in the observed frequency $f(t)$ of the signal. Further effects such as the gravitational redshift and time dilation due to motions of objects in the Solar System ('Einstein' delay) or the propagation of the pulsed signal through curved spacetime ('Shapiro' delay) can become relevant [37, 38]. At this point, we do not take these into

Special Orbit Positions	Explanation
periastron P	Point of closest distance of objects in binary system
ascending node Ω	Position when the neutron star is within the tangent plane and moving away from Earth
Orbital Parameter	**Explanation**
P_{orb}	Orbital period of the pulsar – the time for one full orbit
a	Semi-major axis of the ellipse describing the orbit
b	Semi-minor axis of the orbital ellipse
e	Eccentricity of the orbital ellipse $e = 1 - b/a$
i	Inclination of the orbital plane with respect to the tangent plane of the sky
$T_{\pi/2}$	Time of ascending node passage
ω	Longitude of periastron – angle between the ascending node and the periastron
M	Mean anomaly – fraction of the orbital period P_{orb} that has passed since the neutron star surpassed the periastron $M = \frac{2\pi(t - T_{\pi/2})}{P_{\mathrm{orb}}}$

TABLE 5.1 – Definition of orbital parameters relevant for the binary correction. For a visual representation of the orbital ellipse parameters, see Figure 5.2 [33, 36, 32].

account, as their impact on neutrino propagation has to be studied further.

5.3 Final Pipeline

We choose to implement the epoch folding analysis in `python` to make it compatible with other tools used in neutrino and multiwavelength astronomy as well as make it easily accessible to a majority of people in the field.

The general functionality of epoch folding is provided by the python package `stingray` [39, 40] which implements standard analysis techniques used in high-energy astrophysics. Our final code uses the `stingray` release version v2.0.0rc1 [41].

Due to incompatibilities with our default `python` version and newer versions of `stingray`, we unintentionally worked with an earlier version v0.3 during the development phase. The main functionality of the Epoch Folding methods is the same for both versions. The only noticeable difference regards the handling of 'good time intervals' (gtis) which correlates to the normalisation of the pulse phase histogram. Although the option for including gtis while performing Epoch Folding was implemented while using v0.3, we noticed that the gtis are internally ignored by the Epoch Folding algorithm in `stingray`. This problem does not appear when using v2.0.0rc1. For reasons still unknown, our implementation of the gtis for v0.3 is not compatible with v2.0.0rc1. Our current version of the analysis pipeline in combination with v2.0.0rc1 produces only NaN values for all χ^2 test statistics. Following the suggestion in the `stingray` documentation that the gtis should be used when the period of the signal is comparable to the size of the gtis, the analysis of the 0 runs and the calculation of the background statistic (see Sect. 6.1) could be performed without the gtis. On the one hand, in this case we are not interested in finding any periodic signal. On the other hand, periods of 'bad' data were significantly shorter than the entire length of each 0-run.

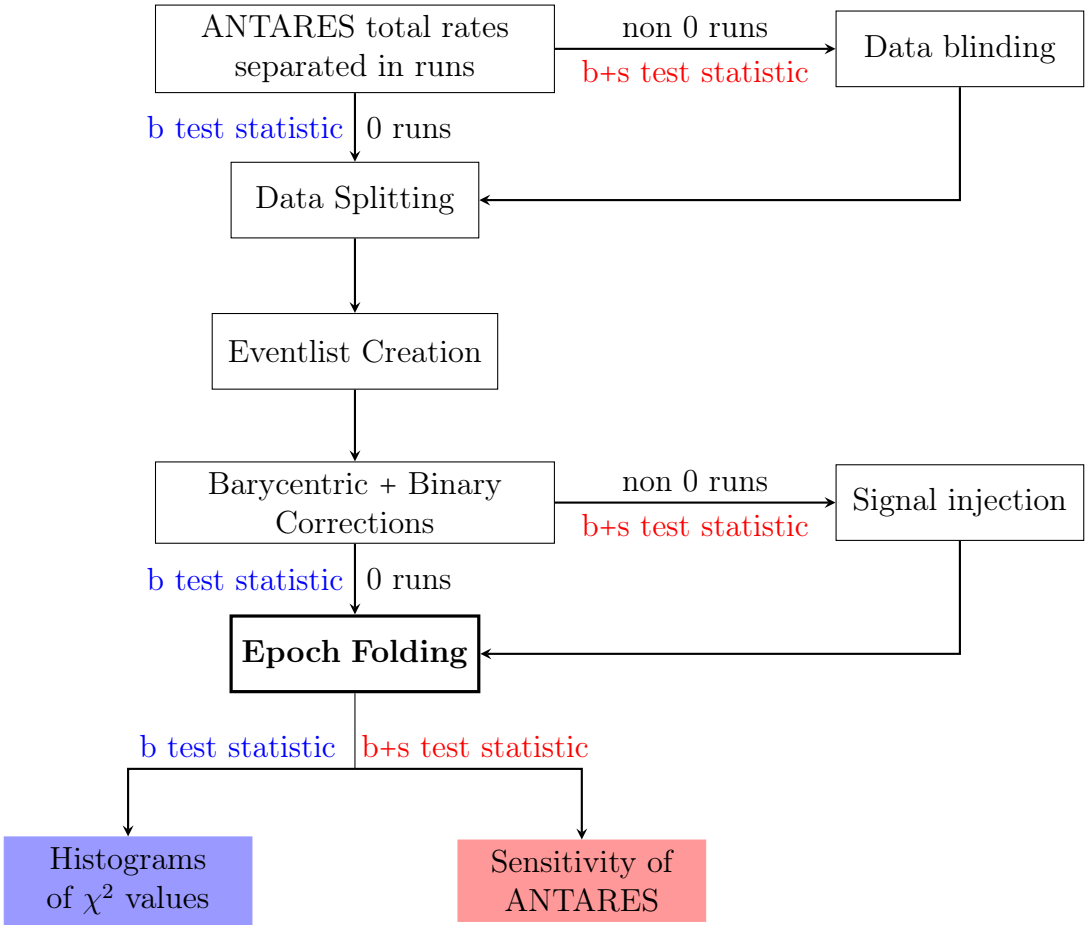

FIGURE 5.3 – General overview over the different steps of the data pre-processing before the Epoch Folding algorithm is applied and the final products of the full pipeline. 'b test statistic' applies to the background-only test statistic calculation (see Sect. 6.1) and 'b+s test statistic' to the background and signal test statistic calculation (see Sect. 6.2).

6 Sensitivity of ANTARES for periodic low-energy neutrinos

The sensitivity of a neutrino telescope can shortly be defined as the minimum flux F for the detection of a signal. In the context of the analysis, it shows the amount of signal, i.e. flux, required to produce a significant deviation on the test statistic χ^2 from the expectation in a background-only hypothesis H_0. This deviation is measured by comparing the probability density function (pdf) of the test statistic in a background-only (b) scenario $f(\chi^2 \,|\, H_0)$, with the pdf of the test statistic for a data sample that contains background and a certain signal strength μ, $f(\chi^2 \,|\, H_\mu)$. Such a comparison can be defined in multiple ways. Here, we perform a goodness-of-fit test [see 42, Chap. 11.1].

Assuming an experiment produces a certain test statistic χ^2_{obs}, the p-value is defined as the probability of observing data as extreme as χ^2_{obs}, assuming that H_0 is true. This can be quantified as

$$p = \int_{\chi^2_{\text{obs}}}^{\infty} f(\chi^2 \,|\, H_0)\, d\chi^2, \tag{6.1}$$

where χ^2_{obs} is the observed value of the test statistic. Such a definition for the p-value is valid for our analysis, where the test statistic is positive and increases with the signal strength (see Eq. (4.8)).

Whether the p-value is large enough to indicate a significant deviation or not, is a subjective decision. Nevertheless, the consensus within the particle physics community is to define a threshold at $p = 2.87 \times 10^{-7}$. This value corresponds to the probability to lay outside a range of 5 standard deviations around the mean of a Gaussian distribution. For this reason, this threshold is also called the 5σ threshold. A p-value equal or smaller than this threshold is considered significant enough to claim a discovery.

The first step to calculate the sensitivity, is to find the threshold value for the test statistic, $\chi^2_{5\sigma}$. The sensitivity of the analysis is then defined by the flux derived from the signal strength μ for which the test statistic χ^2_{obs} is above the threshold $\chi^2_{5\sigma}$ with a probability of 90 %. Formally, this can be written as finding the set of signal strength values μ which satisfy:

$$\int_{\chi^2_{5\sigma}}^{\infty} f(\chi^2 \,|\, H_\mu)\, d\chi^2 \geq 0.9 \tag{6.2}$$

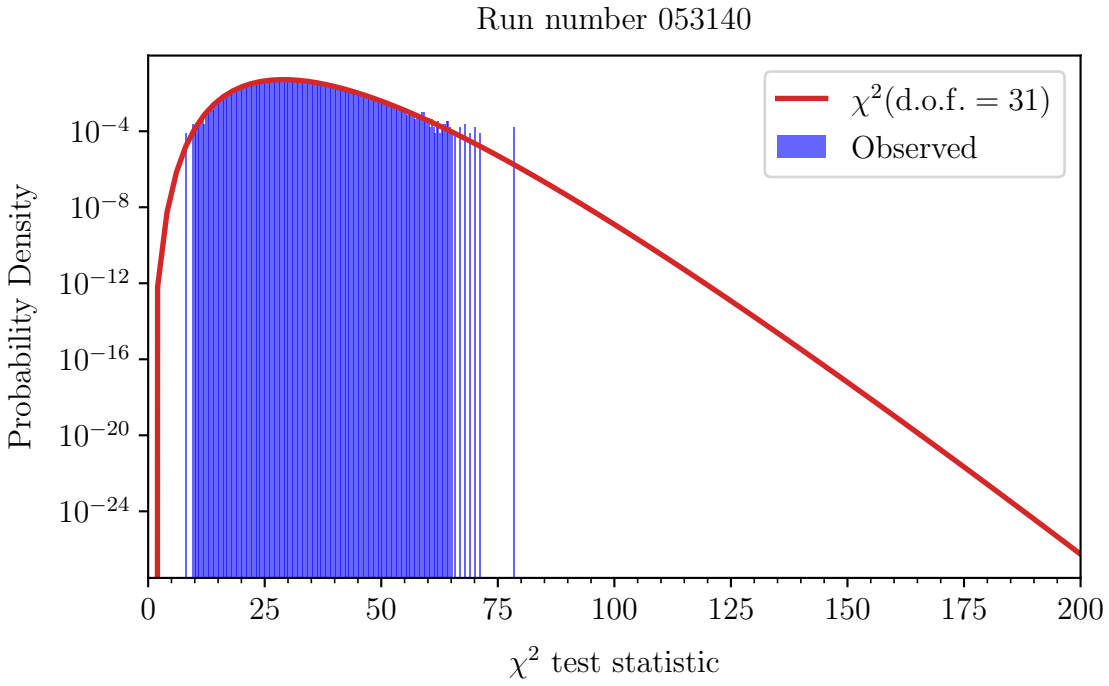

FIGURE 6.1 – Histogram of calculated χ^2 values (see Equation (4.8)) for a number of test-frequencies for run number 053140. The red line shows the theoretical χ^2 distribution for d.o.f. = $N_{\text{bin}} - 1$, where $N_{\text{bin}} = 32$ – the number of bins in the pulse phase histogram.

6.1 Background Test statistic

As described in Section 3.1, the optical background for ANTARES cannot be quantified. To investigate the behaviour of the ANTARES background in the Epoch Folding analysis, we analyse the 0 runs (see Sect. 5.1) for a number of test-frequencies around an arbitrary principal frequency where no periodic signal is expected. As we are using the χ^2 test statistic to evaluate whether a periodic signal is present in the dataset, the χ^2 landscape of a Gaussian-noise-dominated data sample around an arbitrary frequency should resemble the theoretical χ^2 distribution [see 43, Chap. 3.11] with d.o.f. = $N_{\text{bin}} - 1$ [see 43, Chap. 10.6.3].

We find that the ANTARES background follows such a χ^2 distribution. The calculated χ^2 for various test-frequencies are shown in Figure 6.1 together with the theoretical χ^2 distribution.

6.2 Background and Signal Test Statistic

To calculate the test statistic $t\chi^2_\mu$ for the case of background (b) and signal (b+s), we first need to generate datasets containing background and a simulated signal of a certain strength μ. Since the ANTARES optical background is difficult to model, we utilise the background from the total rates of the data-taking period that we want to analyse (see Sect. 6.4). In order to follow the general analysis guidelines of the ANTARES collaboration (see Sect. 5.1) and remove any possible real periodic signal present in the ANTARES rates, we produce a new lightcurve by exchanging the times in the original lightcurve. In this way, the average counting rate stays the same as in the real data, but any possible periodic signal becomes unrecognisable. Subsequently, following our pipeline (see Fig. 5.3), we generate events from the time-shuffled lightcurve. We introduce a periodic signal by introducing additional events following a periodic time distribution. We use a modified von Mises distribution described in detail in the following Section 6.2.1.

As we encountered problems while retrieving the ANTARES dataset for the desired time period, it was not yet possible to calculate the sensitivity. The development of the necessary software, however, to perform this calculation was the main object of this work and has been successfully achieved. As an example, we show Figure 6.2 illustrating the maximal observed test statistic χ^2 and its corresponding p-value (see Eq. (6.1)) for the b+s scenario for different signal strengths μ.

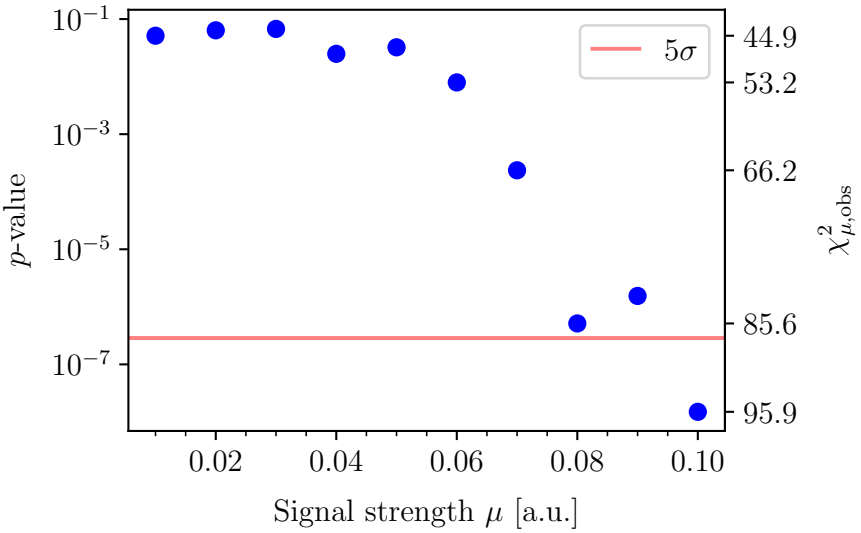

FIGURE 6.2 – p-values and observed χ^2 test statistics for various signal strengths μ. The theoretical χ^2 distribution has 31 degrees of freedom. The fluctuations in the p-values arise from calculating each p-value with only one simulation run for demonstration purposes.

6.2.1 modified von Mises distribution

To describe the shape of the X-ray (and radio) pulses from pulsars, the modified von Mises Distribution (MVMD) is used [44]:

$$f_{\mathrm{MVMD}}(t; f, \kappa) = a \cdot \frac{\exp\left(\kappa \cos\left(2\pi f t + \phi\right)\right) - \exp\left(-\kappa\right)}{I_0(\kappa) - \exp\left(-\kappa\right)} \tag{6.3}$$

where t is the time, f the frequency of the signal, ϕ its phase, κ the shape parameter of the distribution, a a constant scaling factor and $I_0(\kappa)$ is the modified Bessel function of zeroth order. The MVMD can be represented as a sum of cosinusoidal functions by expanding the exponential [44, and reference therein]:

$$\exp\left(\kappa \cos x\right) = I_0(\kappa) + 2\sum_{h=1}^{\infty} I_h(\kappa) \cos\left(2\pi h f t + h\phi\right) \tag{6.4}$$

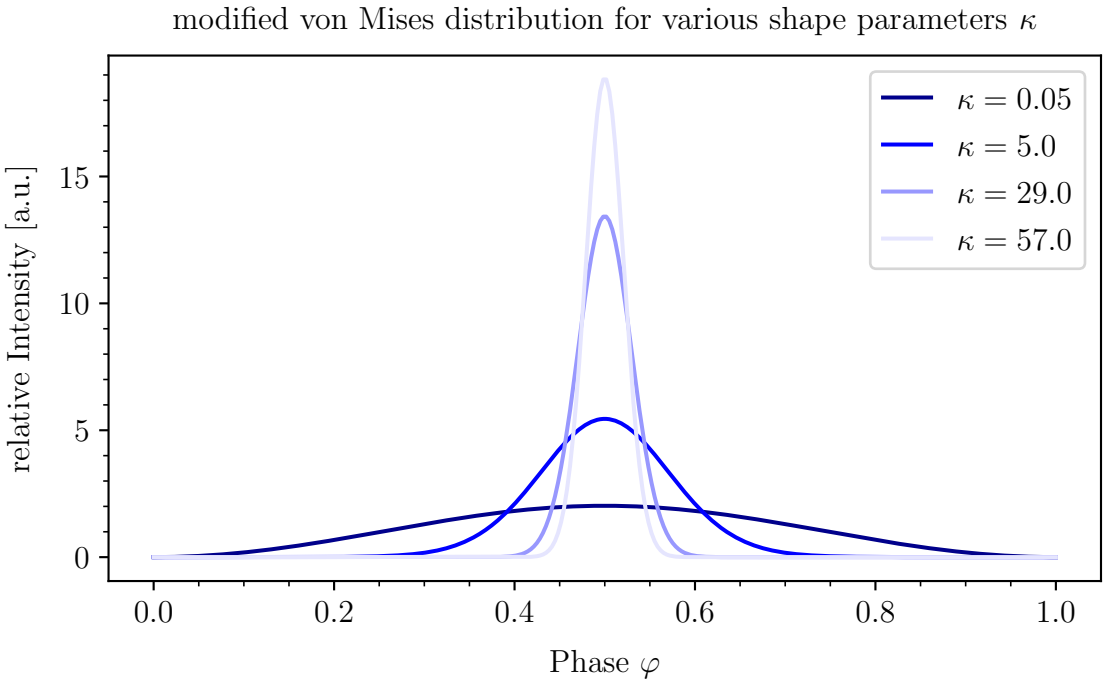

FIGURE 6.3 – MVMD for different values of the shape parameter κ. In the limit of $\kappa \to 0$ the pulse profile is approximated by a sine function, whereas for $\kappa \to \infty$ it converges to a Gaussian [44].

where $I_h(\kappa)$ denotes the modified Bessel function of h-th order. Then the MVMD becomes [44]:

$$f_{\mathrm{MVMD}}(t; f, \kappa) = a + \frac{2a \sum_{h=1}^{\infty} I_h(\kappa) \cos\left(2\pi h f t + h\phi\right)}{I_0(\kappa) - \exp\left(-\kappa\right)} \tag{6.5}$$

In the limit of $\kappa \to 0$ the pulse profile is approximated by a sine function, whereas for $\kappa \to \infty$ it converges to a Gaussian (see Fig. 6.3). We adopt the same pulse shape for the signal injection. Using the inverse cumulative distribution method (see [43]) we draw photon arrival times from the MVMD.

6.3 Relationship between the number of detected events and an incoming neutrino flux

The relationship between the number of detected events $n_\nu(E)$ and a neutrino flux $F_\nu(E)$ can be obtained from the effective volume $V_{\mathrm{eff}}(E)$, which is analogous to

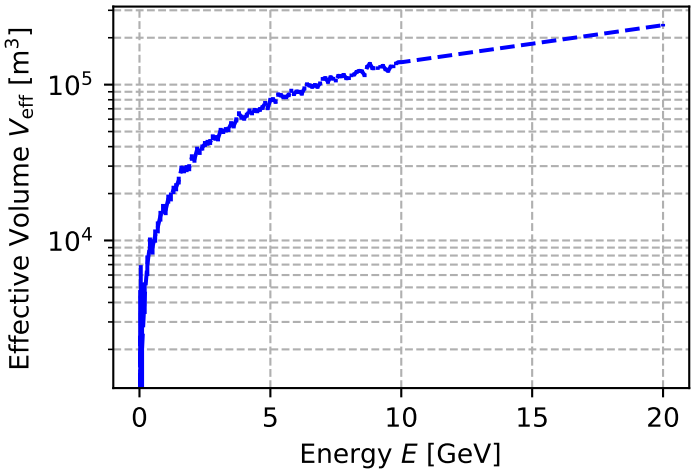

FIGURE 6.4 – Effective volume $V_{\text{eff}}(E)$ of an ANTARES OM as a function of the neutrino energy E.

the effective area $A_{\text{eff}}(E)$ defined in Section 2.3:

$$n_\nu(E) = F_\nu(E) \cdot \sigma_{\nu N}(E) \cdot N_{\text{A}} \cdot \varrho \cdot V_{\text{eff}}(E) \cdot \varepsilon, \tag{6.6}$$

where $\sigma_{\nu N}(E)$ denotes the total neutrino-nucleon cross section, N_{A} the Avogadro constant, ϱ the detector medium density (for ANTARES, the water density) and ε the detector efficiency.

The effective volume has been calculated through simulations where a number of neutrino interactions N_{sim} have been simulated in a volume V around the detector. The effective volume is then defined as follows:

$$V_{\text{eff}}(E) = V \cdot \frac{N_{\text{det}}(E)}{N_{\text{sim}}}\,. \tag{6.7}$$

A detected event N_{det} is an event which produced at least one hit in a PMT. Figure 6.4 shows the effective volume $V_{\text{eff}}(E)$ of an ANTARES OM as a function of energy E.

Equation (6.6) allows the calculation of the number of expected events $n_\nu(E)$ as a function of incoming neutrino flux $F_\nu(E)$ and neutrino energy E. Figure 6.5 illustrates the neutrino detection rate $n_\nu(E)$ of ANTARES as a function of $F_\nu(E)$ and E. The sensitivity can be portrayed in Figure 6.5 by adding a curve representing the required neutrino flux $F_\nu(E)$ to produce a 5σ significance.

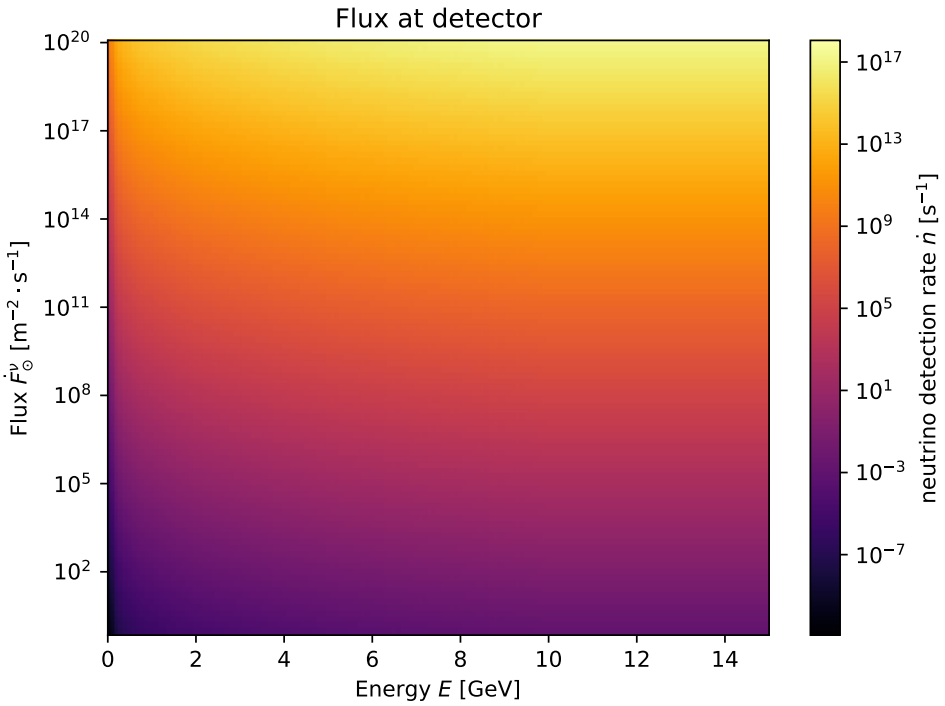

FIGURE 6.5 – Neutrino detection rate $n_\nu(E)$ of ANTARES as a function of neutrino flux $F_\nu(E)$ and neutrino energy E. The sensitivity can be portrayed by adding a curve representing the required neutrino flux $F_\nu(E)$ to produce a 5σ significance.

6.4 Neutrinos from X-ray pulsar Swift J0243.6+6124?

We will apply our Epoch Folding pipeline to existing ANTARES data in order to calculate the sensitivity for a periodic neutrino signal. We choose a period for which the neutrino flux from a binary pulsar is predicted to be the highest. Following [22] this source is Swift J0243.6+6124. Figure 6.6 shows the predicted neutrino lightcurve in comparison to the measured X-ray lightcurve. The maximal predicted neutrino flux at Earth is $F_\nu = 1.2 \times 10^{-2}\,\mathrm{MeV\,cm^{-2}\,s^{-1}}$ around 58070 MJD (modified julian date) [22]. For the periodic signal search, we will focus on the period between approximately 58040 (October 2017) and 58170 MJD (February 2018) where the neutrino flux is predicted to be the highest.

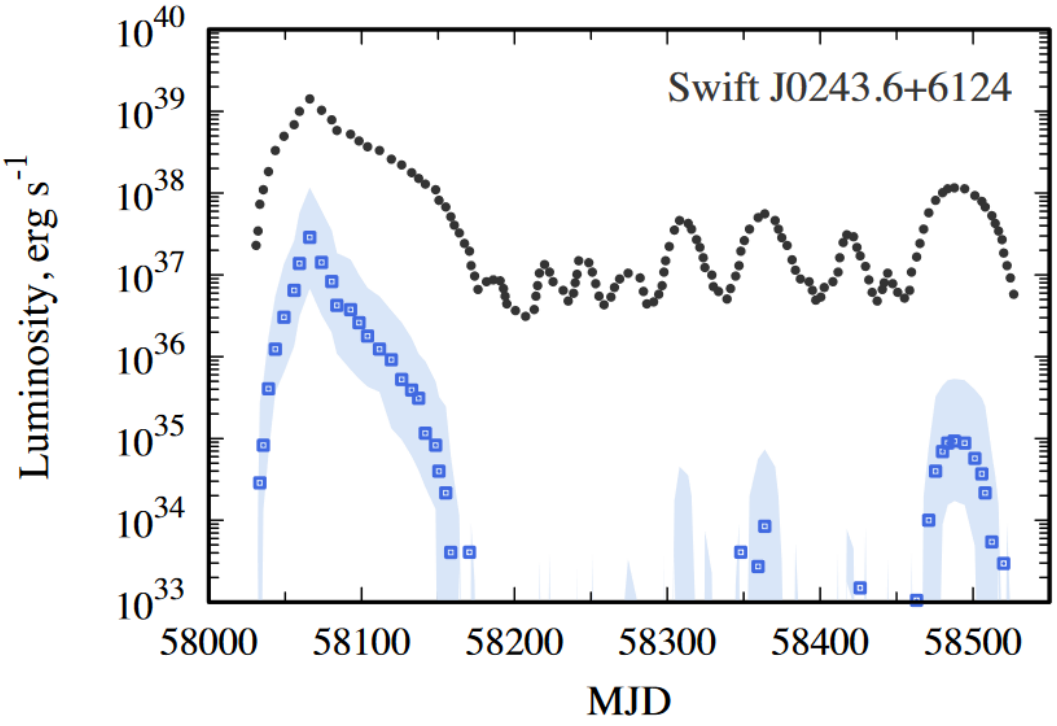

FIGURE 6.6 – X-ray lightcurve of pulsar Swift J0243.6+6124 (black circles). Blue squares depict the neutrino lightcurve predicted by [22]. The point of highest neutrino luminosity $L_\nu = 5.7 \times 10^{37}\,\mathrm{erg\,s^{-1}}$ around 58070 MJD translates to a neutrino flux at Earth of $F_\nu = 1.2 \times 10^{-2}\,\mathrm{MeV\,cm^{-2}\,s^{-1}}$.

7 Summary

The greatest obstacle for performing Neutrino Astronomy from Earth is the Earth's atmosphere. Cherenkov radiation is not only produced by cosmic neutrinos and their secondaries, but also atmospheric neutrinos and muons originating from CR-matter interactions in the Earth's atmosphere. Moreover, the detector medium comprises further challenges. Bioluminescence and potassium-40 decay produce additional optical background for detectors in water like ANTARES or KM3NeT. Various analysis methods have been developed to eliminate this unwanted signal.

The sensitivity of neutrino telescopes to a given neutrino flux depends on the energies of the interacting neutrinos. In general, the sensitivity reduces with decreasing energy as less-energetic secondaries also generate less Cherenkov photons. Most neutrino telescopes are designed to detect neutrinos in the TeV energy range. In this work, we explore the possibility of identifying low-energy neutrinos in high-energy neutrino telescopes. As the optical background is the dominant signal in a neutrino telescope, low-energy neutrinos would be identifiable if they produce a pattern unlike the optical background. We investigate the possibility of detecting periodic signals in the counting rates of the photomultiplier tubes on time scales of variable astrophysical sources. The literature provides us with binary pulsars as possible objects which could produce periodic neutrino flux.

The search for periodic signals in ANTARES data has already been performed using the Fast Fourier Transform (FFT). Here, we implement a new algorithm using a method from high-energy astrophysics, namely Epoch Folding, to achieve the same goal. The idea of Epoch Folding is conceptually very simple: the dataset is divided into sections ('epochs') with a certain period and the signals in each section are added ('folded'). If the test-frequency corresponds to the actual frequency of the signal, the periodic signal is amplified, whereas the noise is averaged out, making it possible to identify the oscillation frequency. If the test-frequency does not correspond to the real period, the folded profile will be averaged to a mean count rate and resemble a 'flat' distribution. Hence, to quantify the presence of a periodic signal, a hypothesis test can be performed in comparing a test statistic (here, χ^2) of various test-frequencies with a constant profile. The largest test statistic value identifies the frequency of the periodic signal.

The major advantage of Epoch Folding compared to the FFT lies in the possibility of analysing large datasets in smaller subsets and adding the single results without loosing detection sensitivity. Furthermore, due to its definition, Epoch Folding is more sensitive to arbitrarily shaped signals compared to the FFT.

Moreover, gaps in the dataset do not require any special treatment as in the case of the FFT. In general, utilising Epoch Folding for a periodic search requires less data pre-processing than with the FFT.

Nevertheless a certain degree of pre-processing is required. We optimise our analysis pipeline for ANTARES counting rates. As the name suggests, the original data products, photomultiplier tube counting rates, are binned. However, Epoch Folding should be performed on un-binned data. Therefore, we generate a so-called 'eventlist' from the binned data under the assumption of uniformly distributed photon hits inside one bin. As described above, due to the very high optical background, the dataset is expected to be large. Consequently, we split the dataset into subsets and rescale the MHz counting rates to enable parallel processing with less computation time. Finally, the relative motion of the observer (Earth) and the emitter (pulsar in a binary system) introduces Doppler shifts in the neutrino arrival times which have to be corrected for precise frequency determination.

The main goal of our Epoch Folding Pipeline is to calculate the sensitivity of ANTARES for a low-energy periodic neutrino flux. The two main problems that remain at the end of this project are, firstly, the current unavailability of the ANTARES rates for the period of the 2017-2018 outburst of X-ray pulsar Swift J0243.6+6124 for which the highest neutrino signal has been predicted in the literature. Secondly, gaps in the dataset should be identified and passed to the Epoch Folding algorithm to achieve accurate results. Currently, the version of our pipeline in combination with the possibility of supplying 'good time intervals' is incompatible with the newest version of the python package `stingray` which provides the basic Epoch Folding methods. For a correct and accurate sensitivity calculation this problem has to be solved before the data for the chosen period is processed with the pipeline. Hence, we cannot provide a sensitivity value at this stage. However, we describe the necessary steps required to obtain the sensitivity utilising our algorithm. Our software can be found on github.

References

[1] Greisen, K., "Cosmic Ray Showers," *Annual Review of Nuclear and Particle Science*, vol. 10, pp. 63–108, Jan. 1960.

[2] Reines, F., "Neutrino Interactions," *Annual Review of Nuclear and Particle Science*, vol. 10, pp. 1–26, Dec. 1960.

[3] Eff, M., "Search for low-energy periodic neutrino sources with ANTARES," Jan. 2023.

[4] Olinto, A.V., "The Origin of the Highest Energy Cosmic Rays," *Relativistic Aspects of Nuclear Physics*, pp. 38–57, Sept. 2001.

[5] Barwick, S. et al, "Neutrino astronomy on the 1 km2 scale," *J. Phys. G: Nucl. Part. Phys.*, vol. 18, p. 225, Feb. 1992.

[6] Ahrens, J. et al, "Sensitivity of the IceCube detector to astrophysical sources of high energy muon neutrinos," *Astroparticle Physics*, vol. 20, pp. 507–532, Feb. 2004.

[7] Collaboration, A., "A Deep Sea Telescope for High Energy Neutrinos." http://arxiv.org/abs/astro-ph/9907432, July 1999.

[8] Adrián-Martínez, S. et al, "Letter of intent for KM3NeT 2.0," *J. Phys. G: Nucl. Part. Phys.*, vol. 43, p. 084001, June 2016.

[9] Belolaptikov, I.A. et al, "The Baikal underwater neutrino telescope: Design, performance, and first results," *Astroparticle Physics*, vol. 7, pp. 263–282, Aug. 1997.

[10] Aynutdinov, V. et al, "The prototype string for the km3-scale Baikal neutrino telescope," *Nuclear Instruments and Methods in Physics Research Section A: Accelerators, Spectrometers, Detectors and Associated Equipment*, vol. 602, pp. 227–234, Apr. 2009.

[11] Katz, U.F. and Spiering, Ch., "High-energy neutrino astrophysics: Status and perspectives," *Progress in Particle and Nuclear Physics*, vol. 67, pp. 651–704, July 2012.

[12] Ruiz, R.G., *Search for Populations of Unresolved Sources of High Energy Neutrinos with the ANTARES Neutrino Telescope*. PhD thesis, Université Sorbonne Paris Cité, Nov. 2016.

[13] Anton, G., "Neutrino Telescopes," in *Probing Particle Physics with Neutrino Telescopes*, pp. 11–32, WORLD SCIENTIFIC, July 2018.

[14] Aloisio, R., Coccia, E. and Vissani, F., *Multiple Messengers and Challenges in Astroparticle Physics*. New York, NY: Springer Berlin Heidelberg, 2017.

[15] Čerenkov, P.A., "Visible Radiation Produced by Electrons Moving in a Medium with Velocities Exceeding that of Light," *Phys. Rev.*, vol. 52, pp. 378–379, Aug. 1937.

[16] Patrignani, C., "Review of Particle Physics," *Chinese Phys. C*, vol. 40, p. 100001, Oct. 2016.

[17] Hale, G.M. and Querry, M.R., "Optical Constants of Water in the 200-nm to 200-Mm Wavelength Region," *Appl. Opt.*, vol. 12, pp. 555–563, Mar. 1973.

[18] Jackson, J.D., *Classical Electrodynamics*. New York: Wiley, 3rd ed ed., 1999.

[19] Heijboer, A., *Track Reconstruction and Point Source Searches with Antares*. PhD thesis, Universiteit van Amsterdam, Amsterdam, The Netherlands, June 2004.

[20] Palladino, A., Spurio, M. and Vissani, F., "Neutrino Telescopes and High-Energy Cosmic Neutrinos," *Universe*, vol. 6, p. 30, Feb. 2020.

[21] Mészáros, P., "Astrophysical Sources of High-Energy Neutrinos in the IceCube Era," *Annu. Rev. Nucl. Part. Sci.*, vol. 67, pp. 45–67, Oct. 2017.

[22] Asthana, A. et al, "Bright X-ray pulsars as sources of MeV neutrinos in the sky," *MNRAS*, vol. 522, pp. 3405–3411, May 2023.

[23] ICECUBE COLLABORATION, "Evidence for High-Energy Extraterrestrial Neutrinos at the IceCube Detector," *Science*, vol. 342, p. 1242856, Nov. 2013.

[24] ICECUBE COLLABORATION, "Neutrino emission from the direction of the blazar TXS 0506+056 prior to the IceCube-170922A alert," *Science*, vol. 361, pp. 147–151, July 2018.

[25] ICECUBE COLLABORATION, "Evidence for neutrino emission from the nearby active galaxy NGC 1068," *Science*, vol. 378, pp. 538–543, Nov. 2022.

[26] ICECUBE COLLABORATION, "Observation of high-energy neutrinos from the Galactic plane," *Science*, vol. 380, pp. 1338–1343, June 2023.

[27] Ageron, M. et al, "ANTARES: The first undersea neutrino telescope," *Nuclear Instruments and Methods in Physics Research Section A: Accelerators, Spectrometers, Detectors and Associated Equipment*, vol. 656, pp. 11–38, Nov. 2011.

[28] Aiello, S. et al, "The KM3NeT potential for the next core-collapse supernova observation with neutrinos," *Eur. Phys. J. C*, vol. 81, p. 445, May 2021.

[29] Mushtukov, A.A. et al, "Ultraluminous X-ray sources as neutrino pulsars," *MNRAS*, vol. 476, pp. 2867–2873, May 2018.

[30] Leahy, D.A. et al, "On searches for pulsed emission with application to four globular cluster X-ray sources : NGC 1851, 6441, 6624 and 6712.," *ApJ*, vol. 266, pp. 160–170, Mar. 1983.

[31] Schwarzenberg-Czerny, A., "On the advantage of using analysis of variance for period search.," *MNRAS*, vol. 241, pp. 153–165, Nov. 1989.

[32] Bissinger, M., *Observations of Be X-ray Binaries: Spin Period and Spectral Evolution*. PhD thesis, Friedrich-Alexander Universität Erlangen-Nürnberg, 2016.

[33] Hilditch, R.W., *An Introduction to Close Binary Stars*. Cambridge: Cambridge University Press, 2001.

[34] Larsson, S., "Parameter estimation in epoch folding analysis," *A&AS*, vol. 117, pp. 197–201, May 1996.

[35] Davies, S.R., "An improved test for periodicity," *MNRAS*, vol. 244, pp. 93–95, May 1990.

[36] Deeter, J.E., Boynton, P.E. and Pravdo, S.H., "Pulse-timing observations of HER X-1.," *ApJ*, vol. 247, pp. 1003–1012, Aug. 1981.

[37] Blandford, R. and Teukolsky, S.A., "Arrival-time analysis for a pulsar in a binary system.," *ApJ*, vol. 205, p. 580, Apr. 1976.

[38] Taylor, J.H. and Weisberg, J.M., "Further Experimental Tests of Relativistic Gravity Using the Binary Pulsar PSR 1913+16," *ApJ*, vol. 345, p. 434, Oct. 1989.

[39] Huppenkothen, D. et al, "Stingray: A modern Python library for spectral timing," *Journal of Open Source Software*, vol. 4, p. 1393, June 2019.

[40] Huppenkothen, D. et al, "Stingray: A Modern Python Library for Spectral Timing," *ApJ*, vol. 881, p. 39, Aug. 2019.

[41] Bachetti, M. et al, "StingraySoftware/stingray: Stingray 2.0.0, release candidate 1." Zenodo, https://doi.org/10.5281/zenodo.10604413, Feb. 2024.

[42] James, F., *Statistical Methods in Experimental Physics*. New Jersey: World Scientific, 2nd ed ed., 2006.

[43] Metzger, W., "Statistical Methods in Data Analysis." https://web2.ba.infn.it/~pompili/teaching/data_analysis_lab/metzger_ediz2010.pdf, Jan. 2010.

[44] Ransom, S.M., Eikenberry, S.S. and Middleditch, J., "Fourier Techniques for Very Long Astrophysical Time-Series Analysis," *AJ*, vol. 124, p. 1788, Sept. 2002.